Applied Energy 280 (2020) 115911

Contents lists available at ScienceDirect

Applied Energy

journal homepage: www.elsevier.com/locate/apenergy

Degradation study of a proton exchange membrane water electrolyzer under dynamic operation conditions

Georgios Papakonstantinou [a,*], Gerardo Algara-Siller [b], Detre Teschner [b,c], Tanja Vidaković-Koch [a,d], Robert Schlögl [b,c], Kai Sundmacher [a,e]

[a] Max Planck Institute for Dynamics of Complex Technical Systems, Process Systems Engineering, Sandtorstr.1, D-39106 Magdeburg, Germany
[b] Fritz Haber Institute of the Max Planck Society, Department of Inorganic Chemistry, Faradayweg 4, D-14195 Berlin, Germany
[c] Max Planck Institute for Chemical Energy Conversion, Department of Heterogeneous Reactions, Stiftstr. 34-36, D-45470 Mülheim an der Ruhr, Germany
[d] Max Planck Institute for Dynamics of Complex Technical Systems, Electrochemical Energy Conversion, Sandtorstr.1, D-39106 Magdeburg, Germany
[e] Otto-von-Guericke University Magdeburg, Process Systems Engineering, Universitätsplatz 2, D-39106 Magdeburg, Germany

HIGHLIGHTS

- Hydrous Ir oxides with sufficient loading cope with fluctuating renewable energy.
- Crystallization induces mild kinetic losses complying with the current targets.
- Small Ir mass losses inside the membrane compared to the anode loading.
- Membrane chemical degradation under dynamic operation causes high resistance losses.
- High but recoverable stationary deactivation by inhibiting or long-lived species.

ARTICLE INFO

Keywords:
PEWE
Dynamic operation
Iridium oxide
Degradation
Recovery
Dissolution/re-deposition

ABSTRACT

Understanding degradation phenomena of polymer electrolyte water electrolyzers operating under dynamic conditions is imperative for developing and implementing efficient and reliable means of energy storage from fluctuating and intermittent renewable energy sources. Herein, a commercial membrane electrode assembly with an amorphous IrO_x anode is subjected to potential sweeping (1.4–1.8 V) with short and long holds and few steady-state interims for overall 830 h at 60 °C and ambient pressure to simulate frequent alternating idle and nominal operation regimes. Systematic electrochemical diagnostics and physicochemical methods are applied to identify degradation sources. Mild kinetic deactivation (2.6 μV/h) is observed independent on the *dynamic* protocol, due to loss of electrochemical surface area via crystallization. The amount of Ir dissolved and redeposited in the ionomer anode phase and in the membrane is negligible in comparison to the current state-of-the-art Ir loadings. As compared to kinetic losses, the irreversible resistive losses are one order of magnitude higher and are thought to be caused by the degradation of the membrane close to the anode catalyst layer. These resistive losses are associated specifically with dynamic operation. The two orders of magnitude higher, but recoverable, degradation during *steady-state* interims is attributed to the growth of inhibiting or long-lived species.

1. Introduction

The increasing share of fluctuating and intermittent renewable energies in the energy sector demands the development of efficient and durable energy storage options. Water electrolysis (WE) is a relatively mature H_2 production technology, suitable to store excess renewable energy produced during off-peak energy demand periods, e.g. during the night or weekends. Among the WE technologies, polymer electrolyte water electrolysis (PEWE) is particularly attractive due to operational benefits, such as high current densities, relatively low energy demand and quick response to grid power fluctuations [1]. However, still efforts

* Corresponding author at: Max Planck Institute for Dynamics of Complex Technical Systems, Process Systems Engineering, Sandtorstraße 1, D-39106 Magdeburg, Germany.
E-mail address: papakonstantinou@mpi-magdeburg.mpg.de (G. Papakonstantinou).

https://doi.org/10.1016/j.apenergy.2020.115911
Received 7 May 2020; Received in revised form 11 September 2020; Accepted 22 September 2020
Available online 1 October 2020

Nomenclature

CV	Cyclic voltammetry
EDX	Energy dispersive X-ray spectroscopy
EIS	Electrochemical impedance spectroscopy
HPT	Hydrogen permeation test
MEA	Membrane electrode assembly
NHE	Normal hydrogen electrode
OC	Open circuit
OCP	Open circuit potential, V
OER	Oxygen evolution reaction
ORR	Oxygen reduction reaction
PEM	Polymer electrolyte membrane
PEWE	Polymer electrolyte water electrolysis
RHE	Reference hydrogen electrode
RT	Room temperature
SEM	Scanning electron microscopy
(S)TEM	(Scanning) transmission electron microscopy
TPR	Temperature programmed reduction
WE	Water electrolysis
XPS	X-ray photoelectron spectroscopy
XRD	X-ray diffraction

List of Symbols

b	Tafel slope, V/dec of current density
C	Capacitance, F/cm^2
E	Potential, V
$E_{HFR\ free}$	HFR free potential, V
HFR	High frequency resistance, Ω.cm^2
i	Current density (vs. geometric area), A/cm^2
i/Q_t	Total voltammetric charge normalized current density, 1/s
Q	Charge, C/cm^2
Q_t	Total voltammetric charge, C/cm^2
t	Time, s or min or h
η	Overpotential, V

are required to understand and address some limitations associated with technological requirements and material properties. The polymer electrolyte membranes (PEM) allow significant permeability of gaseous products [2] that decreases the efficiency and raises safety issues [3] especially under imbalanced pressure operation [4]. The harsh oxidative and corrosive environment (high electrochemical potential and low *pH*) necessitates the use of noble metal based electrocatalysts and Ti current collectors and separator plates, contributing significantly to system's cost [5]. Therefore, enhanced durability is essential, as extended lifetime can compensate for the high investment cost. Understanding the degradation modes of the individual system components, their interplay and the association with specific operating conditions are crucial for enhancing the durability of the whole system.

Most of the knowledge on the degradation of the abundantly used perfluorosulfonic acid membranes comes from the research on PEM fuel cells [6]. Although the operating conditions are different, i.e. higher pressure [4], higher electrochemical potentials and liquid water presence [7] in PEWEs, similar degradation modes are thought to occur [8]. Mechanical degradation can arise from uneven stress and non-proper assembling, while thermal degradation may be induced by sudden temperature gradients [8]. Chemical degradation is assigned to cross-permeation and mixing of H_2 and O_2 that leads to H_2O_2 formation through the $2e^-$ oxygen reduction reaction (ORR) in the cathode [6]. H_2O_2, in the presence of impurity ions from the balance of plant, mostly stainless steel based H_2O supply reservoirs, tubes, etc. [9], decomposes to reactive radicals that attack the PEM [10]. In addition, cations with lower mobility than H^+ can screen sulfonic acid groups and affect H^+ transport [11]. A similar type of degradation is thought to be applicable for the H^+ conducting ionomer [12], which binds the electrocatalyst, extends H^+ conduction in the catalyst layers and tunes the hydrophilic/hydrophobic properties for efficient gas transport and H_2O retention without blocking electron transport [13].

The current collectors/porous transport layers and separator plates are prone to degradation too. To overcome H_2 embrittlement of the Ti separators in the cathode, expensive Au coatings are employed [14]. Ti offers the best compromise between conductivity, corrosion resistance and strength [15], but its surface passivates with a protective oxide layer [16], increasing the contact resistance with the anodic catalyst layer over time [9]. Pt coatings decrease the degradation rate by more than one order of magnitude [9], although they may suffer from exfoliation at high current densities (>2 A/cm^2) [17].

Due to the high roughness factors of Pt/C catalysts, their high Pt loading and low intrinsic overpotential [18], Pt/C cathodes pose little stability concerns even at high current densities [17] and low loadings [19]. Nevertheless, ultra-low Pt loadings might create a risk on long-term stability [20]. However, the kinetics of the oxygen evolution reaction (OER) is sluggish and high overpotentials ($\eta \approx$ 250–350 mV) are required to achieve acceptable reaction rates [21]. Ir oxides are the current state-of-the-art anodes, representing the best trade-off between activity and stability [22], which anti-correlate; stability increases from metallic to quasi-amorphous oxohydroxides to thermally prepared crystalline oxides, while activity decreases across this series [23]. Meanwhile the electrochemical potential [24] and the operation type [25,26] affect stability, with Ir dissolution being the primary cause of instability in aqueous acidic media [27]. The considerable dissolution rates reported with flowing electrolytes [27] have created concerns on the lifetime of Ir based anodes. Based on the stability numbers (moles of O_2 generated/moles of Ir dissolved) published in [28], a PEWE anode with 1 mg/cm^2 loading of hydrous IrO_x nanoparticles would be completely dissolved in ca. 4–5 days when operated at 1 A/cm^2 (1 A/mg), whereas the lifetime of rutile IrO_2 extends up to 1 year.

Operating PEWE cells show however long lifetimes [29,30]. Rutile IrO_2 catalysts with current loadings (>1 mg/cm^2) are very stable, without any evidence of Ir dissolution under stationary operation [9,14]. The kinetic deactivation was attributed to contamination of the anodic active sites by Ti, either from the anodic porous transport layer or from TiO_2 being part of the catalyst. Ir dissolution detected with Ir black anodes [5] is considerable at low loadings (≤0.4 mg Ir/cm^2) [31]. Ir concentrated at the catalyst layer/PEM interface, but also deposited inside the PEM with a gradient along its thickness. The loss of Ir was exacerbated with small IrO_x nanoparticles and ultra-low Ir loadings (0.08 mg Ir/cm^2) [20,32]. Even Ir migration and deposition in the cathode were observed [20].

Dynamic operation with rutile IrO_2 and high loadings mainly affected the cell resistance [14,33], depending on the maximum current density applied and the number of on/off cycles [14]. Slight Ir dissolution and precipitation inside the PEM in close proximity to the anode was detected after intermittent operation with high current densities, pressurized cathode and thin membrane [33]. It was attributed to the reduction of the IrO_2 surface by the permeated H_2 under open circuit and its re-oxidation/dissolution upon re-entering OER potentials. However, significant surface area losses were observed with low loaded IrO_2 anodes (0.1–0.32 mg/cm^2), subjected to solar type or stepped current density (0–2 A/cm^2) profiles at 60 and 80 °C, respectively [34]. A metallic Ir anode (0.1 mg/cm^2) showed 50% kinetic activity loss after 23.000 potential cycles between 1.45 and 2 V at 80 °C [26].

Widely different degradation rates are reported (0–200 μV/h) in the literature, depending on catalyst type, loading and operating conditions

(Table S1 in the Supplementary Material). Degradation typically enhances with current density (potential) and temperature [17,35]. Noble metal coatings decrease the resistive degradation strongly [14]. However, conflicting results are reported under intermittent and dynamic operation. Particularly, dynamic operation does not seem to be problematic with rutile type IrO_2 electrodes and current high loadings [14,17], but the stability of metallic Ir formulations with low loadings is questionable [26,31]. On the other hand, intermittency seems to be challenging for the cathode in the absence of protective inert gas purging [36], while open circuit potential (*OCP*) under enhanced H_2 permeation is not recommended even for rutile type anodes at elevated T (80 °C) [33].

In this work, the stability of an IrO_x-based commercial membrane electrode assembly (MEA) is studied under dynamic conditions (1.4–1.8 V) for 830 h in a mid-sized (63.5 cm^2) all Ti electrolysis single cell at 60 °C and ambient pressure. In addition, short steady-state interims are conducted to explore the temporal responses and compare with those during dynamic operation. Electrochemical diagnostics are systematically employed to analyze the performance evolution with time and distinguish and quantify different degradation phenomena. Pristine and aged MEAs are subjected to in-depth microscopic analysis to understand the structural and chemical changes imposed by potential cycling and identify degradation routes. Commercial anodes with high hydrous IrOx catalyst loadings withstand highly dynamic operating conditions with acceptable kinetic induced degradation. However, potential excursions close to OER onset seem to affect the reaction selectivity inducing chemical degradation of the H^+ conducting network at and close to the anode/PEM interface.

2. Materials and methods

2.1. Materials, single cell and experimental setup

A HYDRion circular MEA (63.5 cm^2 active area, Ir based anode, Pt based cathode, N117, ION POWER) was placed in an all Ti commercial single cell (Sylatech Analysetechnik, type ZE 200) and tightened with 35 Nm torque per bolt (8 bolts). The single cell is large enough to approach real application operating conditions, but at the same time small enough to apply detailed analysis methods. Sintered fibrous Ti-porous transport layer (1 mm thickness, 80% porosity, Sylatech Analysetechnik) with sized gradient fibers in the anode (45 and 20 μm, fine side faces the catalyst layer), and hydrophobized carbon paper (H2315 I6, 210 μm thickness, Freudenberg), along with a woven carbon cloth (700 μm, Sylatech Analysetechnik) in the cathode, were used as porous transport layers. Ti micro-grid expanded metal (7 Ti 10–050, 0.9 mm thickness, Dexmet) served as anode spacer to facilitate reactants/products distribution in the absence of machined channels. More details on the single cell and the commercial test set-up (FuelCon) can be found in the Supplementary Material (Fig. S1) and elsewhere [37].

High purity H_2O (0.055 μS/cm) was re-circulated (50–130 ml/min, measured ex-situ volumetrically) between a heated container and the anode compartment, and served as reactant and heating/cooling medium (cell exposed to the environment). The temperature of the anode inlet H_2O stream was controlled and those at the outlet and middle of the anode plate were recorded. The cathode was always flooded with dry H_2 or N_2 (150–250 ml/min), the former to maintain a well-defined cathode potential (close to 0 V vs. reference hydrogen electrode, RHE) during cyclic voltammetry (CV) measurements, the latter to avoid mixing of H_2 with air back-diffusing from the cathode outlet during start-up/shut-down instances, as well as during low current density operation in the absence of backpressure. A Solartron 1287A potentiostat and a 1250B frequency response analyzer were connected in parallel to the single cell and the 2-quadrant load (0.03–100 A, FuelCon) for CV (load disconnected) and electrochemical impedance spectroscopy (EIS, load connected) measurements. EIS was also performed by short-circuiting the cell without MEA before and after the electrochemical tests to measure the cell hardware resistance (Fig. S2).

2.2. Electrochemical experiments

The assembled cell underwent the cyclic electrochemical operation and diagnostic protocol depicted in Fig. 1. First, the MEA was subjected to a H_2 permeation test (HPT) at room temperature (RT), during which the initial integrity of the cell assemblage as well as the H_2 permeation properties of the PEM were assessed (details on the method in [37]). After a couple of polarization measurements at RT, the electrolyzer was heated up to 60 °C while simultaneously increasing OER polarization in current density steps, followed by initial diagnostics (Fig. 1b and S3). Two long-term dynamic and a few shorter stationary operating interims were applied during 830 h testing at 60 °C. The dynamic protocol consisted of potential sweeping (100 mV/s, 1.4–1.8 V) with respective holds with different dwell times: 1.5 and 2.5 min at 1.4 and 1.8 V, respectively, for 430 h (named as fast protocol and marked with F in Fig. 1a), and 15 min holds at each potential for 315 h (slow protocol, marked with S in Fig. 1a). Detailed potential profiles complemented with the respective current density and temperature responses are shown in Fig. S4. The dual dynamic protocol aimed to disentangle the effects of the number of potential cycles (6560 in fast vs. 630 cycles in slow protocol) and dwell time. Stationary overnight interims in galvanostatic and potentiostatic modes (only the former are shown) at ca. 1.6–1.62 V were explored at the initial testing stage (10.5–66.5 h, shaded areas marked with SS in Fig. 1a), as well as one potentiostatic interim at 1.8 V after dynamic operation, in order to capture the temporal behavior under steady-state. Their duration was short enough to not influence the overall degradation, but sufficient to get insights into the differences between dynamic and stationary operation.

Due to the increase of H_2O conductivity over time in the absence of an ion-exchanger (max. conductivity 5 μS/cm, measured ex-situ in the water drain by a SevenGo-pro conductivity meter, Mettler Toledo), the continuous operation was interrupted every 2–5 days in order to exchange H_2O in the anode recirculation loop. During interruptions, the cell cooled down to RT. Before the H_2O refreshing steps, the diagnostics listed in Fig. 1b were sequentially applied. Specifically, the cathode gas atmosphere was switched from N_2 to H_2 and EIS was performed at the upper potential of the applied protocol. After interrupting the protocol and a short period of *OCP* (≤15 s), three CV cycles were collected starting from the apparent *OCP* (=1.4 V) and sweeping to 0.5 V and backward. Stepwise galvanostatic polarization measurements in both anodic and cathodic directions were adopted as metric of the overall performance, along with EIS at selected current densities to provide for high frequency resistance (*HFR*) free potentials ($E_{HFR\ free}$). After three additional CV cycles, H_2O exchange was performed with the cathode flushed with N_2, followed by a H_2 permeation test at RT. 1.5 CV cycles were then measured at RT and the operating protocol was resumed after raising the temperature again to 60 °C and by stepwise increasing OER polarization. Note that the transient cooling/heating regimes lasted ca. 3 h. At selected intervals, marked with vertical dashed lines in Fig. 1a, CVs with different sweep rates (1–30 mV/s) were recorded to inspect the voltammetric charge dependence on the sweep rate in a fixed potential window (0.5–1.35 V) as metric of the catalyst active area [38]. Slow sweeping is necessary to capture the slow H^+ diffusion within the highly loaded commercial porous electrodes.

2.3. Physicochemical characterization

The phase analysis of the pristine and aged MEAs was done by X-ray diffraction (XRD) in a transmission diffractometer (X-ray STOE STADI P). Scanning electron microscopy (SEM) was performed on the electrodes in plain view in a Hitachi S4800 instrument. For optical microscopy characterization (Keyence VHX-5000) the samples where cut in cross-sections, embedded in a resin and polished. Synchrotron ($h\nu$ = 615 eV) based X-ray Photoelectron Spectroscopy (XPS) was used to

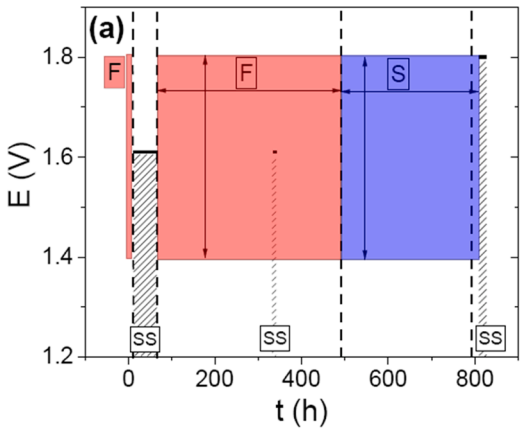

(b)

EIS & protocol interruption (15 s OC*)
Cyclic Voltammetry (CV), 10 mV/s, OCP to 0.5 V, 3 cycles
Up & down (U/D) galvanostatic i-E with EIS
CV, 10 mV/s, OCP to 0.5 V, 3 cycles
** 6 x CVs, 1-30 mV/s, 0.5-1.35 V, 3 cycles each
N_2 purge & H_2O exchange (OCP & cooling to RT)
*** H_2 permeation test at RT (OCP)
**** CV, 10 mV/s, OCP-1.4 V, 2 cycles, RT

* OC = open circuit, OCP = OC potential
** 4 times in total, marked with vertical dashed lines
*** When more than 2 h, OCP < 0.5 V, 7 times in total
**** Only when OCP < 0.5 V

Fig. 1. (a) Operating modes vs. time of operation (refer to the web version for color identification). F (pink region) denotes the fast protocol, S (blue) the slow protocol and SS (dashed) the steady-state interims. All at 60 °C and ambient pressure. (b) List of in-situ diagnostics regularly applied at selected interims. Respective *i*, *E* profiles in Fig. S3.

analyze the chemical composition of the catalyst layers of the pristine and used MEAs. The samples for (scanning) transmission electron microscopy, (S)TEM, and energy dispersive X-ray spectroscopy (EDX) were prepared by microtomy, with the MEA embedded in a resin block and cut with a diamond knife to an electron transparent thickness. (S)TEM characterizations were performed in a JEOL JEM-ARM200F and FEI Talos F200X microscopes, both operated at 200 kV.

3. Results and discussion

3.1. Initial electrochemical responses

CV was applied to inspect the anode catalyst fingerprint in the potential region preceding OER. The initial CV responses at RT, after subjecting the MEA to a HPT (black lines), and after a polarization measurement (red lines), are shown in Fig. 2a. The permeated H_2 slowly drives the *OCP* to low values (=0.03 V). In the CV after HPT, the potential was swept from *OCP* to 1.4 V and backward. The number of cycles was limited to 2.5 in order to prevent cathodic dissolution of Ir [24,25]. The negligible Faradaic processes below 0.4 V and the broad redox features at higher potentials (H^+ injection/ejection processes) are characteristic of hydrous Ir oxides [39]. The excess anodic charge in the first sweep can be related to sites interacted with molecular H_2. Temperature programmed reduction (TPR) of X-ray amorphous Ir oxohydroxides including commercially available IrO_x [40,41] showed consumption of H_2 already at RT. This is not accompanied by H_2O release, suggesting that H_2 is not de-oxygenating the catalyst, but rather remains adsorbed at RT in form of hydroxyls and/or adsorbed H_2O. The lack of excess anodic charge in the second sweep is due to the fact that in the first cathodic sweep (2.3 min duration) solely H^+ injection occurred. Reduction is hindered below 0.4 V as the oxohydroxide is largely switched off by the high resistivity at low potentials [42].

The CV collected after the first polarization measurement is embedded in Fig. 2a (red line). In this case, the excess cathodic charge, appearing only in the first cathodic sweep, is due to the more oxidized, and thus more de-protonated, nature of the catalyst after OER. Two things should be mentioned in comparison to the CV after HPT; i) the reduction of the anodic charge in the second CV cycle after HPT (~35%) was similar to the reduction of the cathodic charge in the second cycle after OER (~31%), and ii) the higher cathodic charge in the second cycle after OER. The former suggests that the same type of catalytic sites is involved in the adsorption of molecular H_2 under open circuit conditions and the de-protonation (catalyst oxidation) during OER conditions. The latter indicates that the catalyst underwent specific changes during the first polarization measurement. In this regard, the transient cathodic charge was measured instantly after OER and regularly throughout the test duration to capture catalyst modifications.

The potential losses in a representative polarization measurement acquired after 66.5 h testing at 60 °C is presented in Fig. 2b (bottom-x, left-y axes). EIS measured at selected current densities (Fig. S5) provided the *HFR free* potential values (magenta portion of the curve). 55% of the potential loss at the maximum current density was resistive, i.e. H^+ and

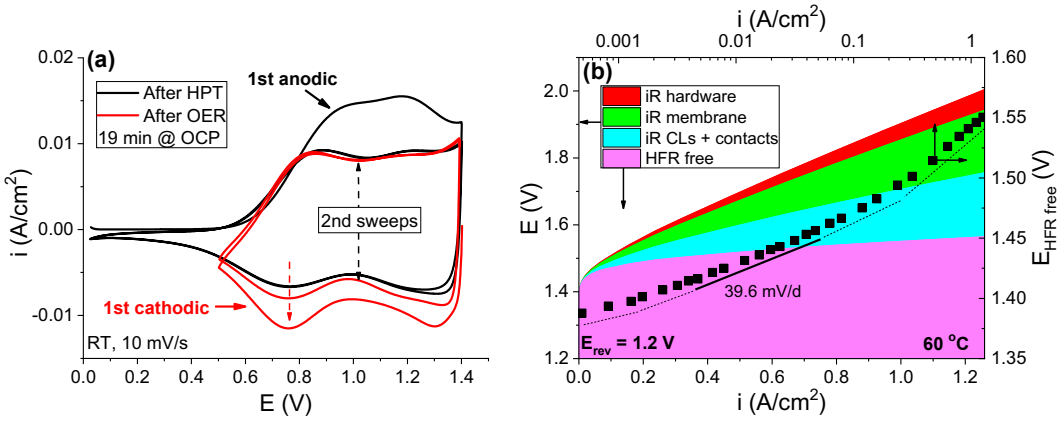

Fig. 2. (a) CVs acquired after HPT (black) and after polarization measurement (red) after cell assembly (RT, 10 mV/s) (refer to the web version for color identification). (b) Potential losses vs. current density (left-y vs. bottom-x axes) and the $E_{HFR\ free}$ vs. current density in log scale (right-y, top-x) in the course of a polarization measurement at 66.5 h (60 °C, ambient pressure).

e^- transport resistances. The cell hardware resistance in MEA absence (red portion) accounts for 7.5%, whereas the H^+ transport resistance through the PEM (green portion), computed with an Arrhenius type relation for fully hydrated N117 [7,43], contributes 23.3%. The remaining 24.3% can be attributed to contact resistances between the catalyst layers and the current collectors.

The $E_{HFR\ free}$ values are plotted against the current density in log scale in Fig. 2b (right-y, top-x axes). Multiple Tafel slopes, i.e. continuous upward bending with increasing current density, were observed, with values ranging from 24 to 80 mV/dec. It should be noted that no further potential corrections were applied, e.g. to account for the H^+ transport resistance in the catalyst layers [44], the influence of gas pressure enhancement (supersaturation) in the catalyst layers on the Nernst potential [37,45], as well as for the influence of H_2 permeation on the current density [37]. The former two contributions increase the apparent slope at high current densities (>0.05 A/cm^2) [37,45], whereas the latter phenomenon skews the slope at low current densities [37]. In the current density regime (5–50 mA/cm^2) where mass transport [13,19] and the above contributions can be neglected, the average slope is ca. 40 mV/dec, which is commonly observed with hydrous Ir oxides [46,47].

3.2. Stability under dynamic conditions

The stability of the MEA is depicted in Fig. 3a, where the current density at 1.8 V during dynamic operation is plotted against time (snapshots of the current density responses at different testing intervals can be seen in Fig. S6). An initial fast activation is observed within the first 10 h of fast cycling. The activation was inhibited during the interim stationary operation at intermediate potentials (1.6–1.62 V, shaded area), and it was resumed during fast cycling with current density plateau at ca. 100–170 h. Thereafter, the current density decayed in an apparently linear fashion with a decay rate of ≈ 85 μA/cm^2/h. The corresponding $E_{HFR\ free}$ values (EIS was not performed at current densities higher than 0.63 A/cm^2 at the initial testing stages) are not changing significantly (dashed black line in Fig. 3a), showing average value of 1.5354 V (standard deviation 0.7 mV).

The constant $E_{HFR\ free}$ with decaying current density after 170 h dynamic operation implies that the apparent degradation has additional kinetic origin. The changes in the mass transport properties can be essentially excluded, as the Tafel slopes of the polarization measurements did not change over the test duration (Fig. S7). To elaborate on the origin of this type of degradation, the current density was normalized to the total voltammetric charge, Q_t, the latter assessed by the charge dependence on the sweep rate (Figs. S8-11, Table S2 and discussion therein) [48]. The charge normalized activity (1.007 ± 0.007 s^{-1}) at 1.8 V ($E_{HFR\ free}$ ≈ 1.535 V) is constant over time (Fig. 3b), which signifies that the observed mild current decay after the activity plateau can be attributed to the loss of the active anodic catalyst surface area. This also indicates that the mode of dynamic operation (fast or slow protocol) does not play a role for the slow deactivation.

The fact that both as measured and *HFR* free potentials were constant with decaying current density does not necessarily mean that the resistive contributions were unaltered with time. In fact, the respective *HFR* values (Fig. 3c) show a mirror imaged profile to the current density; an initial decrease and concomitant increase in apparently linear fashion with a slope $dHFR/dt$ = 43.5 (±2.5) μΩ.cm^2/h. Hence, both *HFR* and kinetics contribute to the overall performance evolution over time, with the respective apparent degradation rates reported in Table 1. Considering the 80 mV/dec Tafel slope at high current density (Fig. 2b & S7b) and the Q_t evolution with time (Fig. S10), we can estimate (see details in the Supplemental Material) the kinetic potential loss (~2.6 μV/h), which is one order of magnitude lower than the degradation due to *HFR*, 32.6 μV/h (=43.5 μΩ.cm^2/h·0.75 A/cm^2). The latter value is lower than values reported under stationary [9], dynamic [14] or accelerated [34] operating conditions at 80 °C with non-coated Ti transport layers. This

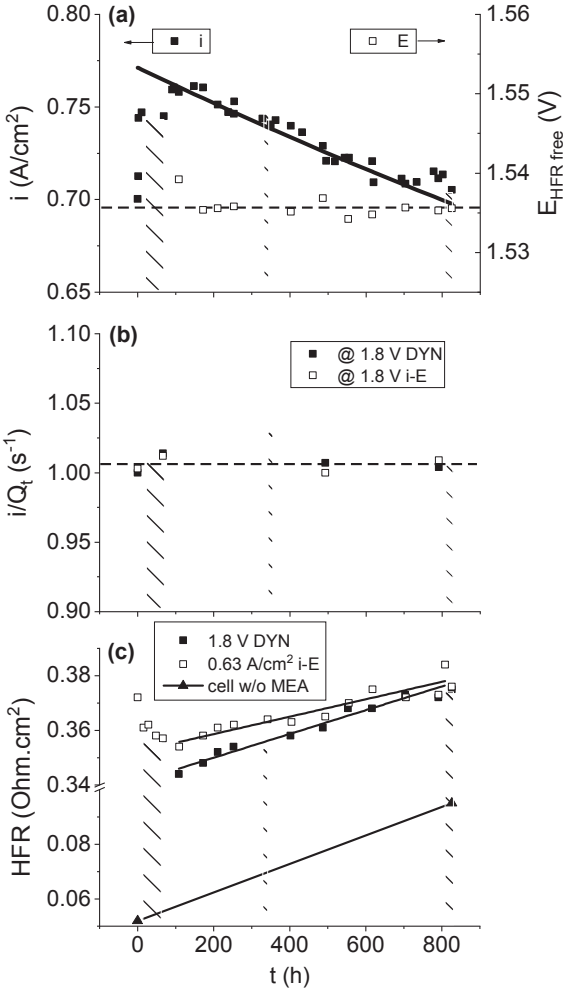

Fig. 3. (a) *i* (solid squares, left-y axis) and $E_{HFR\ free}$ (hollow squares, right-y axis) at 1.8 V during dynamic operation vs. testing time. (b) Current density at as measured 1.8 V during dynamic operation (solid squares) and polarization measurements (hollow squares) normalized to the Q_t vs. testing time. Q_t assessed by CVs with different sweep rates (see Fig. S8). (c) *HFR* at 1.8 V during dynamic operation (solid squares) and at 0.63 A/cm^2 during polarization measurements (hollow squares) vs. testing time. The cell resistance before and after test (solid triangles) is also included. The dashed regions indicate the interims with steady state operation (Fig. 1a). (60 °C, 80–120 ml/min H_2O, ambient pressure).

Table 1
Summary of degradation rates and the targets set by FCH-U for flexible operation.

Type of degradation	Kinetic		Resistive		Total	FCH-JU targets ***	
	μV/h	μA/cm^2/h	μV/h	μΩ·cm^2/h	μV/h	Year	μV/h
Dynamic	2.6	−85	32.6	43.5	35.2	2023	< 4.6
Projected*	0.6					2030	< 2.3
Steady-state**	~ 650		−280	−889	~ 370		
Hardware				52.1			

* Average of projected values to 100.000 h.
** Within 20 h maximum (recoverable).
*** Our calculations based on proposed 1 & 2% efficiency degradation [49].

can be possibly assigned to the lower temperature, $E_{HFR\ free}$ and current density in the present experiment. Furthermore, the rate of *HFR* increase is in relative agreement with the rate of increase of the cell hardware resistance (determined in the absence of MEA, 52.1 μΩ.cm^2/h, Table 1 & Fig. 3c). This suggests that the majority of performance losses comes from the increase of the contact resistance of the Ti based components over time, e.g. anodic catalyst layer/Ti-porous transport layer/Ti-grid/Ti-plate, without excluding the cathodic Ti plate [9,17].

3.3. Predicting degradation under dynamic conditions

Starting from the cell potential balance and accounting for the apparent *HFR* linearity over time (Fig. 3c) as well as the constant $E_{HFR\ free}$ (Fig. 3a), a phenomenological dependence of current density on time can be derived (Eq. (1), details on the derivation in the Supplemental Material).

$$i(t) = i(0)\cdot HFR(0)/\left(\frac{dHFR}{dt}\cdot t + HFR(0)\right) = 0.263/\left(43.5\cdot 10^{-6}\cdot t + 0.341\right) \quad (1)$$

Neglecting the initial activation below ca. 100 h, Eq. (1) describes well the near linear decrease of current density over the experimental time scale (solid line in Fig. 3a). At longer times a nonlinear, decreasing decay (Fig. 4, black line) and rate (Fig. 4, blue line) are expected.

Commonly in literature, the potential and not the current density degradation rate is provided. Assuming that the degradation phenomena are the same in both potentiostatic and galvanostatic conditions, the overpotential change over time under galvanostatic conditions can be derived (Eq. (2)) (details in the Supplemental Material).

$$\eta(t) = \left(\frac{b}{2.303}\right)\cdot\log\left(\frac{dHFR(t)}{dt}\cdot t + HFR(0)\right) + \eta(0) \quad (2)$$

It increases logarithmically with time (Fig. 4) with decaying derivative (i.e. slowing degradation rate) over time (Eq. S10). Similar to the current density decay (Eq. (1)), the overpotential increase is dictated by the *HFR* increase over time, predicting an average degradation rate 2.75 μV/h at 0.75 A/cm^2 in the first 800 h (inset in Fig. 4), in excellent agreement with that deduced from Q_t decay. Projection to 100.000 h (Fig. 4, red line), generates an average degradation rate of ca. 0.6 μV/h (Table 1). The current EU targets set for flexible operation [49] are fulfilled with the present experimental conditions, but only with respect to electrocatalysis (Table 1). To minimize degradation, both *HFR* and *dHFR/dt* should be as low as possible.

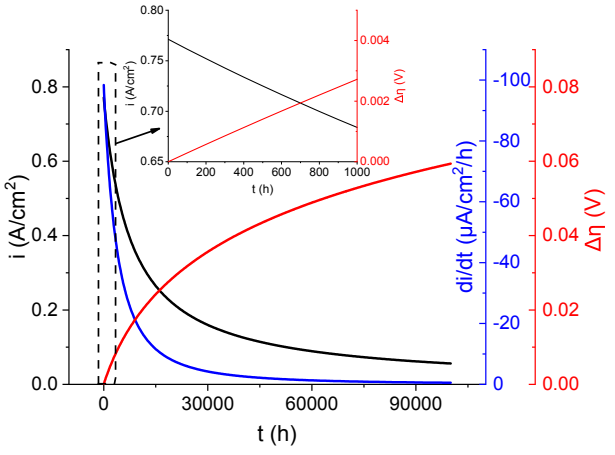

Fig. 4. Plots of Eq. (1) (left-y axis, black), the derivative of current density against time (Eq. S4) (right-y axis, blue) and Eq. (2) vs. time, projected to 100.000 h (refer to the web version for color identification). The inset is zoom-in of the first 1000 h.

3.4. Steady-state interims – Recoverable decay

Whereas acceptable kinetic degradation was observed under dynamic conditions, the apparent degradation rates during stationary interims were 2 orders of magnitude higher (Table 1). This is also shown in Fig. 5a, in which the $E_{HFR\ free}$ values over the time of operation are displayed during two consecutive steady-state interims at 0.315 A/cm^2 (28.5–66.5 h), interrupted by CV (Fig. 5b) and polarization measurements (not shown). The performance losses were completely recoverable after current interruption [9,29] and CV. Fig. 5a is complemented with the *HFR* evolution during the steady-state interims, which reproducibly decreased with time and increased after interruption and CV, anti-correlating with the $E_{HFR\ free}$.

To help understanding of the aforementioned phenomena, the first (solid lines) and second (dashed lines) cathodic sweeps after 18 h at 0.315 A/cm^2 (time: 48.5 h; final $E_{HFR\ free}$ = 1.51 V, final black points in Fig. 5a) and after CV and 7 min at the same current density (time 48.6 h; $E_{HFR\ free}$ = 1.497 V, second red points in Fig. 5a) are compared in Fig. 5b. A profound effect of time at OER potentials on the first cathodic sweep is observed, whereas the second sweeps are nearly identical. While the low potential cathodic charge, located over the broad peaks at ca. 0.75 and 1.1 V, is very similar, the high potential cathodic peak (at ca. 1.3 V) grows with time under steady-state OER. The *OCP* decreases with time at open circuit conditions between current interruption and CV (Fig. S12), consequently decreasing the charge of the high potential peak. However, the overall cathodic charge divided by the CV potential window (thus the pseudo-capacitance, $Q/E = C$) is essentially the same for open circuit dwell times up to 19 min at RT (Fig. S12). Therefore, the species oxidized during OER and involved in the H^+ injection at low potentials (roughly < 1.2 V) show high retention time, likely including changes of the substrate (subsurface) in view of the 3D character of IrO_x in OER electrocatalysis [50,51]. Note that the broadness and intensities of the peaks at 0.75 and 1.1 V are comparable. On the other hand, the high potential peak is significantly narrower, indicating more surface or close to surface character. We suggest that the high potential peak involves the reduction of either (i) long-living OER intermediates, likely preceding the rate determining step, being stable enough to be observed after 15 s at *OCP*, and/or (ii) OER side-products that inhibit the reaction kinetics. Their increasing population with time at steady-state is accompanied by *HFR* decrease and intensive deactivation (Fig. 5a), signifying the interrelation of these quantities.

The OER induced surface is protonated upon cathodic sweeping to low potentials, forming hydroxyls [52]. Such hydroxylation, for example of the oxo-bridging ligands, decreases the electronic coupling between the Ir centers [52] and can increase the electric resistance. Alternatively, the adsorbed oxygen containing intermediates or higher surface oxides [53] are reductively stripped by CV. The activity is then fully restored, due to the regeneration of Ir sites with lower valence [50,54], accompanied by HFR increase in apparently revertible manner (Fig. 5a). In contrast, the activity drops significantly slower during dynamic operation (Table 1). The transient cathodic current upon sweeping down to 1.4 V during dynamic operation (Figs. S4 & S13) impedes the growth and even lowers the population of stable OER intermediates or inhibitor species (Fig. 5b and S14) and the activity is partially retained. Full recovery takes place only after regeneration of the IrO_x by CV, i.e. low potentials (Fig. S15).

3.5. Post-test analysis

Extensive physico-chemical characterization was performed on the catalyst coated membranes to better understand other potential sources of deactivation, apart from the loss of active electrochemical surface area.

A macroscopic surface comparison of the pristine and aged anodic catalyst layers (Fig. S16) reveals the presence of grooves (ca. 20–30 μm wide) from the Ti transport layer formed after assembling and testing.

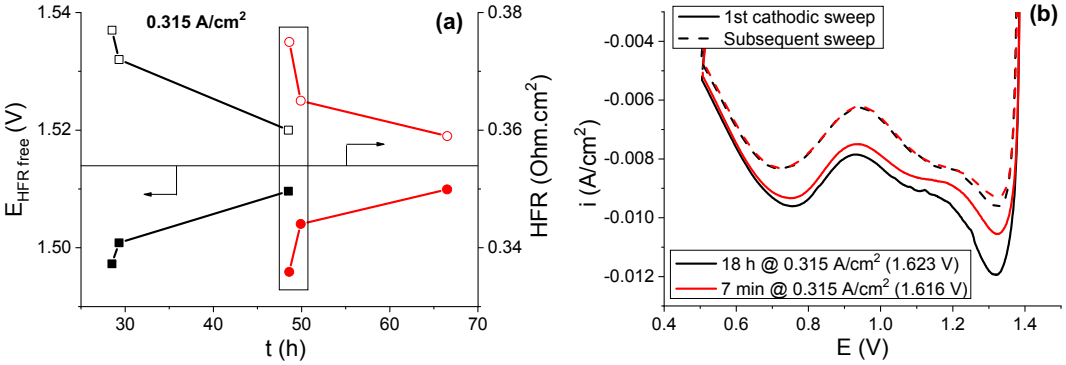

Fig. 5. (a) $E_{HFR\ free}$ (left-y axis, solid symbols and lines) and *HFR* (right-y axis, open symbols) vs. accumulated operating time, measured during two intermittent galvanostatic steady-state operations at 0.315 A/cm^2, with 15 s *OCP* and 3 CV cycles (0.5–1.4 V) in between (first interim in black and concomitant in red). (b) Effect of time under steady-state on the cathodic voltammetric sweeps after current interruption and 15 s *OCP* (60 °C, ambient pressure) (refer to the web version for color identification).

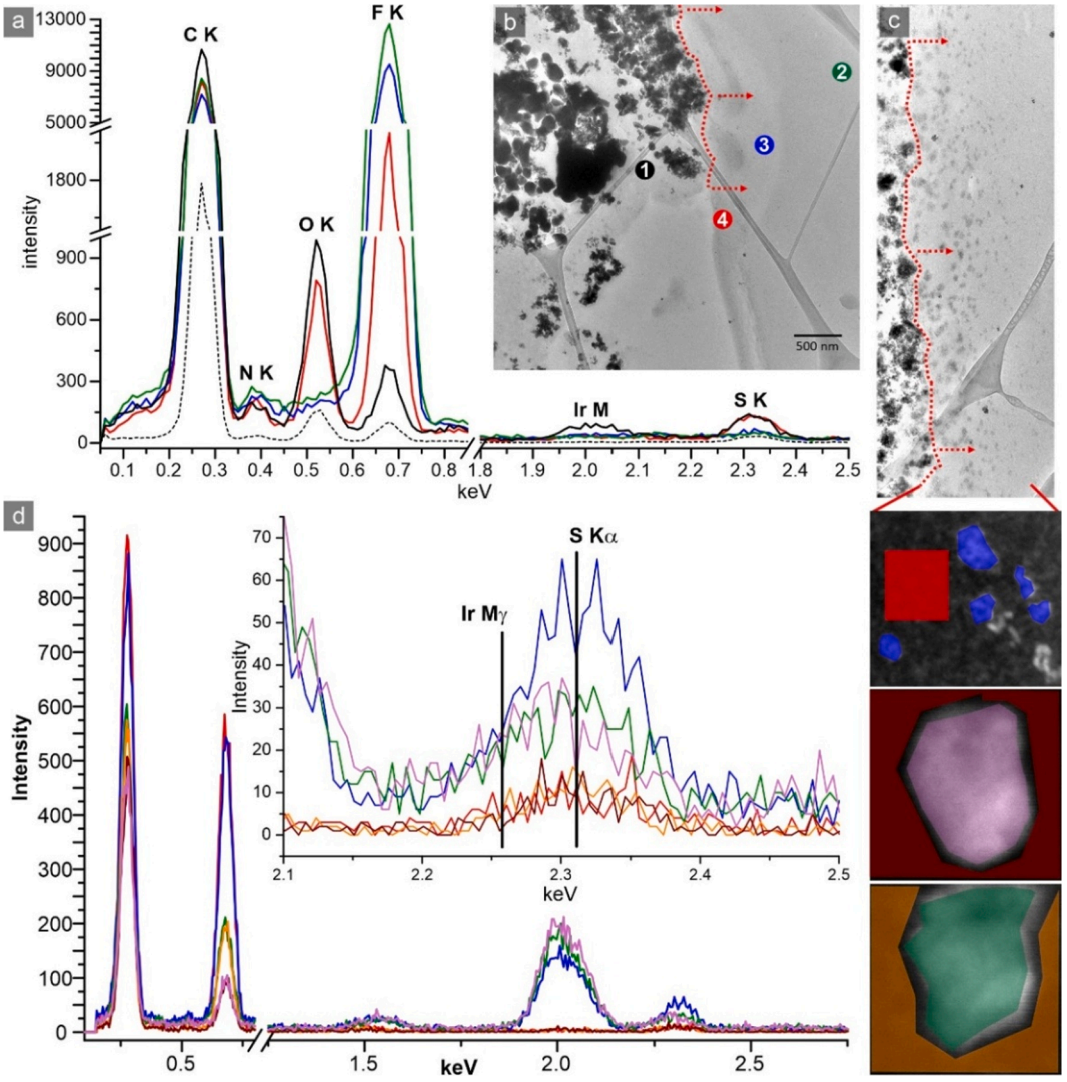

Fig. 6. (a) EDX spectra at different locations of the aged anode and PEM (refer to the web version for color identification). The exact positions of the EDX acquisition are marked in (b) with the same color as that of the respective spectra. The dashed EDX line is the average of the ionomer phase in the pristine anode (see also Fig. S25). (c) HRTEM image showing a band of material within the PEM extending up to 1 μm (the width of the image is 1 μm). The material is found to be Ir particles containing Sulphur as seen in the STEM EDX spectra in (d). Width of STEM images in (d) from top to bottom, 54.4 nm, 11.5 nm and 11.5 nm. The colored STEM EDX spectra correspond to the colored STEM image areas. The red dashed line in (b) and (c) schematically indicates the PEM and anode coating interface. Note, (c) is not directly part of (b).

This limited contact between the porous transport layer and the anode coating can explain the high initial resistive contributions observed in Fig. 2b [55].

The thickness of the catalyst layers on both sides of the PEM seems to be unaffected by the operation (Figs. S18 & Table S3) and the estimated metal loadings (e.g. > 1.1 mg Ir/cm^2, Table S4) are high enough to prevent any extensive degradation.

XRD and microscopic phase analysis (Figs. S20-23) suggest that the anode is predominantly amorphous IrO_x beside a minority (few μm sized) metallic Ir phase. After testing, i.e. upon 830 h operation, nano-crystalline hollandite and rutile IrO_2 phases appear in low quantity. Crystallization is thought to be accompanied by the loss of total electrochemical charge (capacitance) [56], thus the ~ 5% loss of total charge can be at least partially related to the observed crystallization. Despite the minor crystallization, a slightly lower average oxidation state (higher Ir^{+3}/Ir^{+4} ratio) is deduced from XPS analysis (Fig. S24).

Comparative analytical TEM characterization of the PEM after careful cross section preparation (microtomy) is used to obtain more information about the physical and chemical consequences of the applied electrochemical protocol on the ionomer and on the PEM. Spot EDX characterization on the ionomer after electrochemical testing shows that the ionomer contains traces of iridium material (Fig. 6a & b). These traces are not evident in the fresh PEM sample (Fig. S25) indicating Ir dissolution and redeposition under (dynamic) operation. The comparison with the pure ionomer and PEM EDX spectra also suggests that these species are oxidized in nature. Furthermore, Ir containing agglomerates and particles are found within the first micrometers of the Nafion membrane adjacent to the anode (Fig. 6c & d), similar to what is reported in literature [20,31]. These sulphur-containing Ir particles, with sulphur originating from the membrane, have negligible oxygen content and are present only in the used PEM. This indicates that the dissolved Ir ions diffuse to the membrane and get reduced by H_2 coming from the cathode. The position of the Ir agglomerates in the membrane close to the anode side indicates a H_2-rich atmosphere (sizable permeation) inside the PEM [33]. These Ir particles are not only a confirmation of dissolution and loss of active material, but also they might cause increase of the proton resistance of the membrane by blocking some of the proton transport pathways, even presenting a potential long-term route of PEM failure by facilitating membrane degradation. An alteration of the PEM chemical composition (decrease of the F content of the Nafion membrane) close to the anode coating (see change of the EDX spectra from spot 2-to-3-to-4 in Fig. 6a), which is not seen in the fresh membrane sample (Fig. S25), is in line with the above proposition.

3.6. Discussion on degradation pathways

The pristine highly porous anode coating is largely heterogeneous on the meso- and nano-scale (Figs. S21b & S23). This is beneficial for O_2 removal and catalyst utilization, the latter evidenced by the high Q_t. Assuming that the charge generating Ir sites face complete transition between (III) and (IV) oxidation states [51] within the CV potential range (0.5–1.35 V) under slow sweeping, the initial Q_t (0.7C/cm^2) corresponds to a loading of ca. 1.4 mg Ir/cm^2, in reasonable agreement with the estimate from the anode thickness (1.1 – 2.4 mg/cm^2). This indicates that the whole anode coating (even deeper part of the anode film) and even bulk sites of the amorphous IrO_x catalyst seem to be accessible to protons [38] (Fig. S9). However, these benefits come at the expense of electron and potentially proton percolation across a thick catalyst layer at high CV sweep rates and high current densities during OER. These facts in conjunction with the high porosity of the Ti-porous transport layer and the limited contact with the catalyst layer (Fig. S16) give rise to high initial resistive losses (Fig. 2b & 3c).

The high catalyst layer thickness (and loading) is advantageous for the stability (only 5% loss of total charge after 7190 potential cycles) by creating long transport pathways for the dissolved Ir species. Since the deposition of Ir seems to be favored at high potential (0.9 – 1.4 V vs. NHE) and low *pH* [57], as evidenced by the atomically dispersed oxidized Ir on the ionomer inside the anode layer, we suspect that most of dissolved Ir is retained in the active reaction zone. Thus, Ir losses towards the Ti-porous transport layer are expected to be low, as the net flow of H_2O is towards the cathode. Some of the dissolved Ir species however diffuse towards the PEM, where they reductively precipitate by the permeating H_2 [33] forming a band of Ir nanoparticles. Although the operating pressure was atmospheric, the Ir-band position indicates the high relative concentration of H_2 inside the PEM, exacerbated at low current densities [37].

The active material lost compared to the anode thickness is small, because we do not observe any measurable thickness change (Fig. S18 & Table S3). In this regard, we assume that the major contribution of the slow deactivation under dynamic operation is related to crystallization, which reduces the electrochemically accessible surface area, as the crystalline material is less active than the amorphous IrO_x [56].

The steady-state deactivation is linked to a species responsible for the high potential cathodic peak (1.3 V). Its regeneration by cathodic reduction was partial during the dynamic operation and full after CV (Fig. S15). If these (electro-)catalytic redox processes not only involve H^+ intercalation, but also bond breaking, it is likely that the released oxygen-containing species will have (hydro-)peroxo- character, due to the high potential that prevents H_2O formation (>1.2 V), unless their concentration is high enough to drive the equilibrium potential of H_2O_2 reduction to H_2O to higher values [58]. In fact, the formation of H_2O_2 and $HO_2^{\cdot}$ as OER by-products on Ir oxides in aqueous acidic electrolyte has been detected under potential sweeping conditions [59]. The latter species (hydroperoxyl radicals) can be further reduced to H_2O_2 (1.44 V vs. NHE) or H_2O and hydroxide radical (1.4 V vs. NHE) [60]. All of these species can contribute Nafion decomposition, possibly catalyzed by the dissolved/deposited Ir species. Note that F loss is specifically observed close to the anode/PEM interface and in presence of Ir (Fig. 6). Consequently, the proton resistance is expected to increase and may contribute to the observed *HFR* increase over time (Fig. 3c). This represents a potential long-term route of PEM failure. Also, the fluoride emission from the PEM should not be overlooked, as it can corrosively react with the Ti based cell components [61] and affect the contact resistance, as indicated by the post-test hardware resistance measurements (Fig. 3c). In these ways, the *HFR* increase observed herein and during intermittent operation of PEM water electrolyzers [14,17] can be realized. Apparently, a stable noble metal coating of the Ti-porous transport layer cannot be presently avoided in order to prevent resistive degradation under dynamic conditions.

4. Conclusions

Overall, the current state-of-the-art anode catalyst layers are robust enough to withstand dynamic operating conditions, although further optimization of the structure and interfaces is required to enhance activity and stability. Concerns raise though when it comes to low loadings. A specific ionomer/membrane degradation route is identified under dynamic operation. The sequential character of different degradation modes is highlighted; the IrO_x catalyst selectivity/stability triggers the chemical ionomer degradation, which may even trigger Ti corrosion, suggesting that an optimized operating mode with small number of potential modulations but with complete anode regeneration can restrain overall degradation and enhance the lifetime. The overall stability of the current membrane electrode assemblies suggests that stability experiments should extend for more than the commonly used 1000 h to allow for reliable predictions. Alternatively, accelerated degradation means are required based on prior knowledge of potential degradation routes aided by physicochemical characterization. We believe that the present work is an important step in this direction.

CRediT authorship contribution statement

Georgios Papakonstantinou: Methodology, Formal analysis, Investigation, Writing - original draft, Writing - review & editing, Visualization. **Gerardo Algara-Siller:** Methodology, Formal analysis, Investigation, Writing - review & editing, Visualization. **DetreTeschner:** Formal analysis, Investigation, Writing - review & editing, Visualization. **Tanja Vidaković-Koch:** Writing - review & editing, Supervision. **Robert Schlögl:** Conceptualization, Writing - review & editing, Supervision, Funding acquisition. **Kai Sundmacher:** Writing - review & editing, Supervision, Funding acquisition.

Declaration of Competing Interest

The authors declare that they have no known competing financial interests or personal relationships that could have appeared to influence the work reported in this paper.

Acknowledgements

The authors acknowledge the MAXNET Energy Consortium of the Max Planck Society and Deutsche Forschungsgemeinschaft (Grant no. SU189/7-1) for the financial support. Prof. A.A. Auer (MPI-KoFo) is thanked for the valuable discussions and careful reading of the manuscript. Sven Reichstein is thanked for his assistance in electrochemical testing. Danail Ivanov, Wiebke Frandsen, Frank Girgdies, Jasmin Allan and Adnan Hammud are here thanked for sample preparation, SEM and XRD measurements.

Appendix A. Supplementary data

Supplementary data to this article can be found online at https://doi.org/10.1016/j.apenergy.2020.115911.

References

[1] Carmo M, Fritz DL, Mergel J, Stolten D. A comprehensive review on PEM water electrolysis. Int J Hydrogen Energy 2013;38:4901–34. https://doi.org/10.1016/j.ijhydene.2013.01.151.
[2] Schalenbach M, Carmo M, Fritz DL, Mergel J, Stolten D. Pressurized PEM water electrolysis: Efficiency and gas crossover. Int J Hydrogen Energy 2013;38:14921–33. https://doi.org/10.1016/j.ijhydene.2013.09.013.
[3] Grigoriev SA, Millet P, Korobtsev SV, Porembskiy VI, Pepic M, Etievant C, et al. Hydrogen safety aspects related to high-pressure polymer electrolyte membrane water electrolysis. Int J Hydrogen Energy 2009;34:5986–91. https://doi.org/10.1016/j.ijhydene.2009.01.047.
[4] Trinke P, Bensmann B, Reichstein R, Hanke-Rauschenbach R, Sundmacher K. Hydrogen Permeation in PEM Electrolyzer Cells Operated at Assymetric Pressure Conditions. J Electrochem Soc 2016;163:F3164–70. https://doi.org/10.1149/2.0221611jes.
[5] Lettenmeier P, Wang R, Abouatallah R, Helmly S, Morawietz T, Hiesgen R, et al. Durable Membrane Electrode Assemblies for Proton Exchange Membrane Electrolyzer Systems Operating at High Current Densities. Electrochim Acta 2016;210:502–11. https://doi.org/10.1016/j.electacta.2016.04.164.
[6] Borup R, Meyers J, Pivovar B, Kim YS, Mukundan R, Garland N, et al. Scientific Aspects of Polymer Electrolyte Fuel Cell Durability and Degradation. Chem Rev 2007;107:3904–51. https://doi.org/10.1021/cr050182l.
[7] Ito H, Maeda T, Nakano A, Takenaka H. Properties of Nafion membranes under PEM water electrolysis conditions. Int J Hydrogen Energy 2011;36:10527–40. https://doi.org/10.1016/j.ijhydene.2011.05.127.
[8] Grigoriev SA, Dzhus KA, Bessarabov DG, Millet P. Failure of PEM water electrolysis cells: Case study involving anode dissolution and membrane thinning. Int J Hydrogen Energy 2014;39:20440–6. https://doi.org/10.1016/j.ijhydene.2014.05.043.
[9] Rakousky C, Reimer U, Wippermann K, Carmo M, Lueke W, Stolten D. An analysis of degradation phenomena in polymer electrolyte membrane water electrolysis. J Power Sources 2016;326:120–8. https://doi.org/10.1016/j.jpowsour.2016.06.082.
[10] Li N, Araya SS, Kær SK. Long-term contamination effect of iron ions on cell performance degradation of proton exchange membrane water electrolyser. J Power Sources 2019;434:226755. https://doi.org/10.1016/j.jpowsour.2019.226755.
[11] Sun S, Shao Z, Yu H, Li G, Yi B. Investigations on degradation of the long-term proton exchange membrane water electrolysis stack. J Power Sources 2014;267:515–20. https://doi.org/10.1016/j.jpowsour.2014.05.117.
[12] Gubler L, Dockheer SM, Koppenol WH. Radical (HO•, H• and HOO•) Formation and Ionomer Degradation in Polymer Electrolyte Fuel Cells. J Electrochem Soc 2011;158:B755–69. https://doi.org/10.1149/1.3581040.
[13] Bernt M, Gasteiger HA. Influence of Ionomer Content in IrO_2/TiO_2 Electrodes on PEM Water Electrolyzer Performance. J Electrochem Soc 2016;163:F3179–89. https://doi.org/10.1149/2.0231611jes.
[14] Rakousky C, Reimer U, Wippermann K, Kuhri S, Carmo M, Lueke W, et al. Polymer electrolyte membrane water electrolysis: Restraining degradation in the presence of fluctuating power. J Power Sources 2017;342:38–47. https://doi.org/10.1016/j.jpowsour.2016.11.118.
[15] Rozain C, Millet P. Electrochemical characterization of Polymer Electrolyte Membrane Water Electrolysis Cells. ElectrochimActa 2014;131:160–7. https://doi.org/10.1016/j.electacta.2014.01.099.
[16] Bystron T, Vesely M, Paidar M, Papakonstantinou G, Sundmacher K, Bensmann B, et al. Enhancing PEM water electrolysis efficiency by reducing the extent of Ti gas diffusion layer passivation. J Appl Electrochem 2018;48:713–23. https://doi.org/10.1007/s10800-018-1174-6.
[17] Rakousky C, Keeley GP, Wippermann K, Carmo M, Stolten D. The stability challenge on the pathway to high-current-density polymer electrolyte membrane water electrolyzers. Electrochim Acta 2018;278:324–31. https://doi.org/10.1016/j.electacta.2018.04.154.
[18] Neyerlin KC, Gu W, Jorne J, Gasteiger HA. Study of the exchange current density for the hydrogen oxidation and evolution reactions. J Electrochem Soc 2007;154:B631–5. https://doi.org/10.1149/1.2733987.
[19] Bernt M, Siebel A, Gasteiger HA. Analysis of Voltage Losses in PEM Water Electrolyzers with Low Platinum Group Metal Loadings. J Electrochem Soc 2018;165:F305–14. https://doi.org/10.1149/2.0641805jes.
[20] Yu H, Bonville L, Jankovic J, Maric R. Microscopic insights on the degradation of a PEM water electrolyzer with ultra-low catalyst loading. Appl Catal B: Environm 2020;260:118194. https://doi.org/10.1016/j.apcatb.2019.118194.
[21] McCrory CCL, Jung S, Ferrer IM, Chatman SM, Peters JC, Jaramillo TF. Benchmarking Hydrogen Evolving Reaction and Oxygen Evolving Reaction Electrocatalysts for Solar Water Splitting Devices. J Am Chem Soc 2015;137:4347–57. https://doi.org/10.1021/ja510442p.
[22] Danilovic N, Subbaraman R, Chang KC, Chang SH, Kang YJ, Snyder J, et al., Activity-Stability Trends for the Oxygen Evolution Reaction on Monometallic Oxides in Acidic Environments, J Phys Chem Lett 2014; 5: 2474–8. https://doi.org/10.1021/jz501061n.
[23] Cherevko S, Geiger S, Kasian O, Kudyk N, Grote JP, Savan A, et al. Oxygen and hydrogen evolution reactions on Ru, RuO_2, Ir, and IrO_2 thin film electrodes in acidic and alkaline electrolytes: A comparative study on activity and stability. Catal Today 2016;262:170–80. https://doi.org/10.1016/j.cattod.2015.08.014.
[24] Cherevko S, Geiger S, Kasian O, Mingers A, Mayrhofer KJJ. Oxygen evolution activity and stability of iridium in acidic media. Part 1. – Metallic iridium. J Electroanal Chem 2016;773:69–78. https://doi.org/10.1016/j.jelechem.2016.04.033.
[25] Cherevko S, Geiger S, Kasian O, Mingers A, Mayrhofer KJJ. Oxygen evolution activity and stability of iridium in acidic media. Part 2. – Electrochemically grown hydrous iridium oxide. J Electroanal Chem 2016;774:102–10. https://doi.org/10.1016/j.jelechem.2016.05.015.
[26] Alia SM, Rasimick B, Ngo C, Neyerlin KC, Kocha SS, Pylypenko S, et al. Activity and Durability of Iridium Nanoparticles in the Oxygen Evolution Reaction. J Electrochem Soc 2016;163:F3105–12. https://doi.org/10.1149/2.0151611jes.
[27] Cherevko S, Reier T, Zeradjanin AR, Pawolek Z, Strasser P, Mayrhofer KJJ. Stability of nanostructured iridium oxide electrocatalysts during oxygen evolution reaction in acidic environment. Electrochem Commun 2014;48:81–5. https://doi.org/10.1016/j.elecom.2014.08.027.
[28] Geiger S, Kasian O, Ledendecker M, Pizzutilo E, Mingers AM, Fu WT, et al. The stability number as a metric for electrocatalyst stability benchmarking. Nat Catal 2018;1:508–15. https://doi.org/10.1038/s41929-018-0085-6.
[29] Siracusano S, Van Dijk N, Backhouse R, Baglio V, Arico AS. Degradation issues of PEM electrolysis MEAs. Renewable Energy 2018;123:52–7. https://doi.org/10.1016/j.renene.2018.02.024.
[30] Ayers KE, Renner JN, Danilovic N, Wang JX, Zhang Y, Maric R, et al. Pathways to ultra-low platinum group metal catalyst loading in proton exchange membrane electrolyzers. Catal Today 2016;262:121–32. https://doi.org/10.1016/j.cattod.2015.10.019.
[31] Zhao S, Stocks A, Rasimick B, More K, Xu H. Highly Active, Durable Dispersed Iridium Nanocatalysts for PEM Water Electrolyzers. J Electrochem Soc 2018;165:F82–9. https://doi.org/10.1149/2.0981802jes.
[32] Yu H, Danilovic N, Wang Y, Willis W, Poozhikunnath A, Bonville L, et al. Nano-size IrOx catalyst of high activity and stability in PEM water electrolyzer with ultra-low iridium loading. Appl Catal B: Environm 2018;239:133–46. https://doi.org/10.1016/j.apcatb.2018.07.064.
[33] Weiss A, Siebel A, Bernt M, Shen TH, Tileli V, Gasteiger HA. Impact of Intermittent Operation on Lifetime and Performance of a PEM Water Electrolyzer. J Electrochem Soc 2019;166:F487–97. https://doi.org/10.1149/2.0421908jes.
[34] Rozain C, Mayousse E, Guillet N, Millet P. Influence of iridium oxide loadings on the performance of PEM water electrolysis cells: Part II – Advanced oxygen electrodes. Appl Catal B: Environm 2016;182:123–31. https://doi.org/10.1016/j.apcatb.2015.09.011.
[35] Suermann M, Bensmann B, Hanke-Rauschenbach R. Degradation of Proton Exchange Membrane (PEM) Water Electrolysis Cells: Looking Beyond the Cell Voltage Increase. J Electrochem Soc 2019;166:F645–52. https://doi.org/10.1149/2.1451910jes.

[36] Grigoriev SA, Bessarabov DG, Fateev VN. Degradation Mechanisms of MEA Characteristics during Water Electrolysis in Solid Polymer Electrolyte Cells. Russian J Electrochem 2017;53:318–23. https://doi.org/10.1134/S1023193517030065.
[37] Papakonstantinou G, Sundmacher K. H2 permeation through N117 and its consumption by IrOx in PEM water electrolyzers. Electrochem Commun 2019;108:106578. https://doi.org/10.1016/j.elecom.2019.106578.
[38] Ardizzone S, Fregonara G, Trasatti S. "INNER" AND "OUTER" ACTIVE SURFACE OF RuO_2 ELECTRODES. Electrochim Acta 1990;35:263–7. https://doi.org/10.1016/0013-4686(90)85068-X.
[39] Gottesfeld S. Faradaic Processes at the Ir/Ir Oxide Electrode. J Electrochem Soc 1980;127:1922–5. https://doi.org/10.1149/1.2130037.
[40] Pfeifer V, Jones TE, Velasco Velez JJ, Massue C, Arrigo R, Teschner D, et al. The electronic structure of iridium and its oxides. Surf Interface Anal 2016;48:261–73. https://doi.org/10.1002/sia.5895.
[41] Pfeifer V, Jones TE, Wrabetz S, Massue C, Velasco Velez JJ, Arrigo R, et al. Reactive oxygen species in iridium-based OER catalysts. Chem Sci 2016;7:6791–5. https://doi.org/10.1039/C6SC01860B.
[42] Glarum SH, Marshall JH. The A-C Response of Iridium Oxide Films. J Electrochem Soc 1980;127:1467–74. https://doi.org/10.1149/1.2129932.
[43] Kopitzke R, Linkous CA, Anderson HR, Nelson GL. Conductivity and water uptake of aromatic-based proton exchange membrane electrolytes. J Electrochem Soc 2000;147:1677–81. https://doi.org/10.1149/1.1393417.
[44] Babic U, Nilsson E, Patru A, Schmidt TJ, Gubler L. Proton Transport in Catalyst Layers of a Polymer Electrolyte Water Electrolyzer: Effect of the Anode Catalyst Loading. J Electrochem Soc 2019;166:F214–20. https://doi.org/10.1149/2.0341904jes.
[45] Trinke P, Keeley GP, Carmo M, Bensmann B, Hanke-Rauschenbach R. Elucidating the Effect of Mass Transport Resistances on Hydrogen Crossover and Cell Performance in PEM Water Electrolyzers by Varying the Cathode Ionomer Content. J Electrochem Soc 2019;166:F465–71. https://doi.org/10.1149/2.0171908jes.
[46] Grimaud A, Demortière A, Saubanère M, Dachraoui W, Duchamp M, Doublet ML, et al. Activation of surface oxygen sites on an iridium-based model catalyst for the oxygen evolution reaction. Nat Energy 2016;2:16189. https://doi.org/10.1038/nenergy.2016.189.
[47] Fierro S, Kapałka A, Comninellis C. Electrochemical comparison between IrO2 prepared by thermal treatment of iridium metal and IrO2 prepared by thermal decomposition of H2IrCl6 solution. Electrochem Commun 2010;12:172–4. https://doi.org/10.1016/j.elecom.2009.11.018.
[48] Trasatti S. PHYSICAL ELECTROCHEMISTRY OF CERAMIC OXIDES. Electrochim Acta 1991;36:225–41. https://doi.org/10.1016/0013-4686(91)85244-2.
[49] Fuel Cells and Hydrogen Joint Undertaking, Multi-AnnualWorkPlan2014-2020, 30/6/2014, http://www.fch.europa.eu/sites/default/files/documents/FCH2%20JU%20-%20Multi%20Annual%20Work%20Plan%20-%20MAWP_en_0.pdf (accessed 30/9/2016).
[50] Massue C, Pfeifer V, van Gastel M, Noack J, Algara-Siller G, Cap S, et al. Reactive electrophilic OI–species evidenced in high-performance Ir-oxohydroxide water oxidation electrocatalysts. Chem Sus Chem 2017;10:4786–98. https://doi.org/10.1002/cssc.201701291.
[51] Saveleva VA, Wang L, Teschner D, Jones T, Gago AS, Friedrich KA, et al. Operando Evidence for a Universal Oxygen Evolution Mechanism on Thermal and Electrochemical Iridium Oxides. J Phys Chem Lett 2018;9:3154–60. https://doi.org/10.1021/acs.jpclett.8b00810.
[52] Pavlovic Z, Ranjan C, Gao Q, van Gastel, Schlögl R. Probing the Structure of a Water-Oxidizing Anodic Iridium Oxide Catalyst using Raman Spectroscopy. ACS Catal 2016;6:8098–105. https://doi.org/10.1021/acscatal.6b02343.
[53] Conway BE, Bourgault PL. Significance of E.M.F. Decay Measurements. Applications to the Nickel Oxide Electrode. Trans Faraday Soc 1962;58:593–607. https://doi.org/10.1039/TF9625800593.
[54] Pfeifer V, Jones TE, Velasco Velez JJ, Arrigo R, Piccinin S, Havecker M, et al. In situ observation of reactive oxygen species forming on oxygen-evolving iridium surfaces. Chem Sci 2017;8:2143–9. https://doi.org/10.1039/C6SC04622C.
[55] Schuler T, Schmidt TJ, Buchi FN. Polymer Electrolyte Water Electrolysis: Correlating Performance and Porous Transport Layer Structure: Part II. Electrochemical Performance Analysis, J Electrochem Soc 2019;166:F555–65. https://doi.org/10.1149/2.1241908jes.
[56] Reier T, Teschner D, Lunkenbein T, Bergmann A, Selve S, Kraehnert R, et al. Electrocatalytic Oxygen Evolution on Iridium Oxide: Uncovering Catalyst-Substrate Interactions and Active Iridium Oxide Species. J Electrochem Soc 2014;161:F876–82. https://doi.org/10.1149/2.0411409jes.
[57] Blakemore JD, Schley ND, Kushner-Lenhoff MN, Winter AM, D'Souza F, Crabtree RH, et al. Comparison of Amorphous Iridium Water-Oxidation Electrocatalysts Prepared from Soluble Precursors. Inorg Chem 2012;51:7749–63. https://doi.org/10.1021/ic300764f.
[58] Katsounaros I, Schneider WB, Meier JC, Benedikt U, Biedermann PU, Auer AA, et al. Hydrogen peroxide electrochemistry on platinum: towards understanding the oxygen reduction reaction mechanism. Phys Chem Chem Phys 2012;14:7384–91. https://doi.org/10.1039/c2cp40616k.
[59] Kuznetsova E, Cuesta A, Thomassen MS, Sunde S. Identification of the by products of the oxygen evolution reaction on Rutile-type oxides under dynamic conditions. J Electroanal Chem 2014;728:102–11. https://doi.org/10.1016/j.jelechem.2014.06.031.
[60] Sawyer DT, Valentine JS. How Super Is Superoxide? Acc Chem Res 1981;14:393–400. https://doi.org/10.1021/ar00072a005.
[61] Wang ZB, Hu HX, Liu CB, Zheng YG. The effect of fluoride ions on the corrosion behaviour of pure titanium in 0.05 M sulphuric acid. Electrochim Acta 2014;135:526–35. https://doi.org/10.1016/j.electacta.2014.05.055.